Applied Mathematical Modelling 138 (2025) 115751

Contents lists available at ScienceDirect

Applied Mathematical Modelling

journal homepage: www.elsevier.com/locate/apm

A thermal flexible rotor dynamic modelling for rapid prediction of thermo-elastic coupling vibration characteristics in non-uniform temperature fields

Yazheng Zhao, Jin Zhou *, Mingjie Guo, Yuanping Xu

College of Mechanical and Electrical Engineering, Nanjing University of Aeronautics and Astronautics, Nanjing, 210016, China

ARTICLE INFO

Keywords:
Thermal flexible rotor
Coupling vibration
Thermal stress
Non-uniform temperature

ABSTRACT

The flexible rotors within aero-engines operate in complex thermal environments, where temperature influences both the vibration frequency and amplitude. This study establishes a simple thermal flexible rotor dynamics model to rapidly and precisely predict thermo-elastic coupling vibration characteristics within a non-uniform temperature field. The thermal potential energy of the thermal rotor element is derived for any temperature field, and the motion equation is obtained using the Euler-Lagrange equation. Specifically, the generalized vector of an arbitrary point and cross-sectional non-uniform thermal stress of the thermal rotor element are considered in the thermal potential energy. The model's frequency error is <1 % under identical boundary conditions. Numerical findings indicate that thermal stress, temperature-dependent material properties, and the coupling effect collectively reduce the natural frequency (NF), with thermal stress having a more pronounced impact under axial constraint. Additionally, thermal stress and material decrease the amplitude across a broad range of rotation speeds, contrasting with thermal bending. This model will play a key role in the iterative calculation of thermo-elastic coupling vibration control due to its accuracy and simplicity.

1. Introduction

High-speed flexible rotors constitute the core of aero-engines, delivering power to rotating equipment. The natural frequency and amplitude of the flexible rotor working at high temperatures are different from those at normal temperature. As the rotating machinery advances into realms of heightened temperatures, the thermo-elastic coupling vibrations in high-speed rotors have garnered significant attention. Its impact on the performance of rotating machinery continues to grow, underlining the critical importance of tackling this intricate challenge. Consequently, enhancing the design efficiency of rotating structures, precise modelling and rapid analysis of vibration characteristics in thermal rotors within high-temperature environments are imperative. Simultaneously, this research serves as a theoretical foundation, providing valuable insights for fault diagnosis and troubleshooting in the realm of rotating machinery.

The flexible rotor is classified as a special beam structure. Addressing the modelling and analysis of vibration characteristics in beams within normal temperatures, current research is categorized into two main approaches: the analytical method and the numerical method. Early investigations typically treated the cantilever blade beam as a bending beam [1–4]. Subsequently, the bending effect in the rotor around the axis was considered [5–7]. Concurrently, scholars have undertaken extensive research on cantilever

* Corresponding author.
E-mail address: zhj@nuaa.edu.cn (J. Zhou).

https://doi.org/10.1016/j.apm.2024.115751
Received 3 March 2024; Received in revised form 27 June 2024; Accepted 2 October 2024
Available online 16 October 2024

Nomenclature

$(X,\ Y,\ Z)$ Fixed coordinate system of rotor
$(x_a, y_a,\ z_a,\ \theta_a,\ \varphi_a)$ Each point coordinate system on the centroid axis of the thermal rotor element
$(u_x,\ u_y, u_z)$ An arbitrary point coordinate system within the thermal rotor element
$\{q\}_s$ Generalized coordinate
Ω Rotation speed
L, l_s Rotor length and element length
$T, \Delta T$ Temperature and temperature difference
$[N(s)], [D(s)], [B(s)], [R(s)]$ Displacement and angle shape function and first order partial differential matrices
ρ_s Density
A_s, I_s Cross-sectional area and area moment of inertia
J_{ds}, J_{ps} Diametral and polar moments of inertia
E_s, G_s Elastic modulus and shear modulus
$K_s^{'}$ Shear coefficient
KE, U, U^M, U^T Kinetic energy and potential energy
$\varepsilon_z, \varepsilon_z^T$ Total axial strain and normal axial strain
σ_z^{Temp} Axial thermal stress
μ_s Poisson ratio
α_s Thermal expansion coefficient
r_o, r_i Outer and inner diameter
N^T, M^T Section's normal force and bending moment
$\Gamma,\ \Gamma_{-1},\ \Gamma_0,\ \Gamma_1,\ \Gamma_2,\ \Gamma_3$ Temperature-dependent parameters of the material and coefficients
k Thermal conductivity
h Convective heat transfer coefficient
q_v Internal heat source
c_p Specific heat at constant pressure
E Finite element domain of the axisymmetric structure
T_3, q_2 Medium temperature and heat flux of the third and second boundary conditions
$l = (i,\ j,\ m)$ An array of nodes for an element
W_i Weight function for node i
$\{T\}^E, \{PT\}^E$ Element temperature vector and temperature load vector
$[KT]^E, [NT]^E$ Element thermal conductivity and heat capacity matrix
$[H]^e$ Shape function of temperature
$[M]^e, [C]^e, [G]^e, [K]_M^e, [K]_b^e, [f]_{unl}^e$ Mass, damping, gyro, mechanical stiffness, and bearing stiffness matrices, and unbalanced force vector of the thermal rotor element

beams [8,9] and composite structural beams [10,11]. The intricacies of composite beams have been dissected through the classical beam theory, first-order shear beam theory, and higher-order shear beam theory, and Carrera unified formulation (CUF) [12-16]. It is noteworthy that the CUF offers a unified framework, enabling the transformation of beams into various classical and higher-order beam theories, such as the Timoshenko beam model, to meet specific requirements. The beam modelling techniques have flourished significantly under normal temperature conditions. Both analytical methods and numerical techniques offer distinct advantages in different aspects.

The aforementioned studies overlook the impact of temperature. The intricate interplay of thermo-elastic coupling introduces distinctive vibration characteristics in beams working in high-temperature environments, setting them apart from those observed under normal temperature conditions. The impact of temperature on beams manifests primarily in two distinct aspects:

(1) Firstly, the localized structural thermal stress and deformation within the beam influence the rotor's potential energy, thereby remolding the stiffness characteristics of the beam [17-38]. Sankar et al. [17] employed a classical beam theory to characterize the thermal stress in beams. Concurrently, other scholars developed the thermo-mechanical coupling beam model, grounded in bending beams [18-20] and first-order shear beams [21-26]. Leveraging the Euler-Bernoulli-Vlasov theory, Simonetti et al. [27] devised a numerical model of thin-walled beams, accounting for the influence of temperature. Furthermore, advancements in higher-order shear deformation beam theory were realized [28]. Thermo-mechanical coupling models for porothermoelastic wave, Cosserat body, shell and plate structures [29-33] were also established. These studies on thermoelastic coupling neglected rotation. Subsequently, researchers have undertaken investigations into the analysis of vibration characteristics in rotating beams subjected to temperature fields [34-38]. In their work, Zhang et al. [34] derived the kinematic equations of the thermo-mechanical cantilever beam based on the nonlinear von Karman strain formula. Zhao and Chiu et al. [35,36] introduced the thermal deformation coefficient. Utilizing the first-order shear deformation theory, Guo et al. [37] developed a cantilever

blade beam model within a thermal environment, incorporating nonlinear shell theory. However, these investigations predominantly concentrate on the thermal impact of a rotating cantilever beam, neglecting the thermal effects associated with axial rotation of the beam. Shabanlou et al. [38] obtained the analytical equation of a rotating cylindrical beam under a temperature field, employing the high-order shear deformation beam theory.

(2) Secondly, variations in temperature-dependent material properties further impact the dynamic characteristics of the beam. Numerous researchers opt for employing temperature-dependent material parameters in lieu of constants. Kim, Kauss and Malekzadeh et al. [39-41] specifically addressed the effects of temperature-dependent material on plate and blade behavior. Acknowledging the influence of temperature-dependent material, a more accurate depiction of the vibration characteristics in a thermal rotating beam emerges. Nevertheless, the exploration of temperature-dependent materials is not a dedicated focus for dynamics field.

The literature review shows that most research has mainly focused on the modelling and vibration control of normal temperature beams and high-temperature cantilever blades. For complex high-temperature rotating beams, the advantages and disadvantages of the several methods are summarized:

(1) Analytical method: Analytical method proves beneficial for the deep understanding of thermoelastic mechanisms. Nevertheless, this approach proves unsuitable for addressing the intricate rotor structures and boundary conditions.
(2) High-dimensional finite element method: While this method boasts accuracy, the computational cost of iterative calculations is relatively high. Although certain methodologies exist to reduce model complexity, introducing temperature effects during this simplification process presents challenges.
(3) One-dimensional finite element method: While one-dimensional models provide simplicity, their oversimplification of thermal boundaries fails to account for the impact of non-uniform temperature gradients.

The objective of our investigation is to develop a thermoelastic rotor model adept at swiftly and precisely predicting thermoelastic coupling characteristics. This requires a harmonious blend of simplicity and accuracy. Should the accuracy of the one-dimensional model be ensured, it stands as a viable strategy for accomplishing our research objective.

Therefore, this study introduces a novel one-dimensional thermal rotor dynamic model that accounts for the influence of non-uniform temperature fields. Specifically, this is achieved by accounting for non-uniform thermal stresses and deformation at any point within the element. This approach circumvents the necessity for oversimplification of thermal boundary conditions. It not only comprehensively captures the impact of non-uniform temperature distribution but also swiftly computes vibration characteristics. This constitutes a significant innovation in this research.

The main contributions of this work are:

(1) An accurate and simple thermal flexible rotor dynamic model is proposed. In modelling, thermal stress and temperature-dependent materials under non-uniform temperature fields are considered.
(2) In the thermal potential energy, the cross-sectional thermal stress within the thermal rotor element and generalized vector of an arbitrary point are considered. This pivotal attribute empowers the model to delineate the complexities of thermal boundaries.
(3) The impacts of temperature on thermal stress, inherent characteristic, and speed-up response are discussed under non-uniform temperature fields.
(4) This study fulfills the demands of engineering complexity and offers a solution for iterative calculations amidst intricate thermal boundaries.

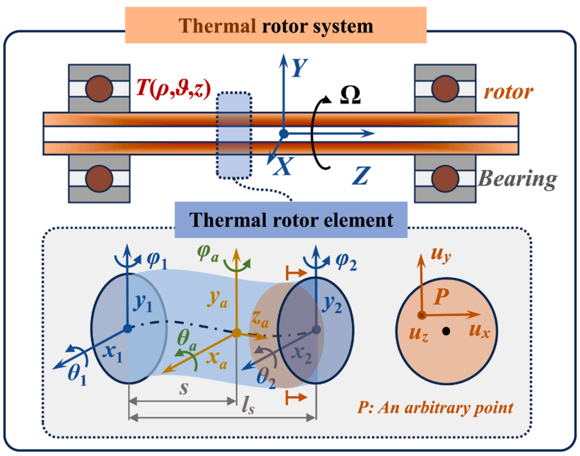

Fig. 1. The coordinate systems of thermal rotor system.

The subsequent sections of this paper are as follows: Section 2 presents a thermal rotor element modelling method. Section 3 introduces the temperature field model. Section 4 delves into the analysis of thermo-elastic coupling vibration characteristics. Section 5 validates the accuracy of the proposed model. Finally, the conclusions are addressed.

2. Mathematic modelling of thermal rotor

Initially, the derivation of the energy equation for the thermal rotor is undertaken, taking into account the assumed boundary conditions. Simultaneously, the temperature dependence of the material is considered. Subsequently, utilizing the Lagrange equation, the finite element motion equation of the thermal rotor is derived. The model exhibits the capability to rapidly and accurately compute the response of the thermal rotor, demonstrating robust engineering applicability.

2.1. Description and assumption of the model

Fig. 1 illustrates the thermal rotor with a length of L around the z-axis at a variable rotation speed $\Omega(t)$. The system experiences the influence of a temperature field, with temperature represented as a function of space—$T(\rho, \vartheta, z)$. The thermal rotor structure is discretized into distinct thermal rotor elements, as shown in Fig. 1. For a thermal rotor element with length l_s, the bending and shear effects are considered.

This model considers four distinct coordinate systems. The thermal rotor is associated with fixed coordinate system (X, Y, Z), whereas each point on the centroid axis of the thermal rotor element is characterized by coordinate system (x_a,y_a,z_a,θ_a,φ_a), and an arbitrary point within the thermal rotor element is defined by coordinate system (u_x,u_y,u_z). Furthermore, the generalized coordinate system for the thermal rotor element is articulated as follows:

$$\{q\}_s = [x_1 \quad y_1 \quad \theta_1 \quad \varphi_1 \quad x_2 \quad y_2 \quad \theta_2 \quad \varphi_2]^{\mathrm{T}}. \tag{1}$$

Point P denotes any location within a general section of the thermal rotor element. In accordance with shear deformation theory, the displacement at the Point P is determined by the displacement of any point along the centroid line of the thermal rotor element:

$$\begin{cases} u_x = x_a, \\ u_y = y_a, \\ u_z = z_a - x\varphi_a - y\theta_a. \end{cases} \tag{2}$$

The displacement, $[x_a, y_a]^{\mathrm{T}}$, at any point along the centroid axis is defined by the displacement shape function matrix $[N(s)]$ and the generalized coordinate $\{q\}_s$. Correspondingly, the rotation angle, $[\theta_a, \varphi_a]^{\mathrm{T}}$, at any point within the element is expressed using the angle shape function matrix $[D(s)]$ and the generalized coordinate $\{q\}_s$:

$$[x_a, y_a, \theta_a, \varphi_a]^T = \begin{Bmatrix} [N(s)] \\ [D(s)] \end{Bmatrix} \{q\}_s, \tag{3}$$

where s represents the distance from the left node i of the thermal rotor element to any section along the axial direction. The shape function matrices $[N(s)]$ and $[D(s)]$ are expressed as follows:

$$\begin{aligned} [N(s)] &= \begin{bmatrix} N_1(s) & 0 & 0 & N_4(s) & N_5(s) & 0 & 0 & N_8(s) \\ 0 & N_1(s) & N_4(s) & 0 & 0 & N_5(s) & N_8(s) & 0 \end{bmatrix}, \\ [D(s)] &= \begin{bmatrix} 0 & D_1(s) & D_4(s) & 0 & 0 & D_5(s) & D_8(s) & 0 \\ D_1(s) & 0 & 0 & D_4(s) & D_5(s) & 0 & 0 & D_8(s) \end{bmatrix}. \end{aligned} \tag{4}$$

Each term in the shape function matrix is a cubic interpolation shape function with respect to s. The specific representation is provided in the Appendix A. The first-order partial derivative matrices of the shape function are defined as:

$$B(s) = \frac{\partial N(s)}{\partial s}, R(s) = \frac{\partial D(s)}{\partial s}. \tag{5}$$

Therefore, the first-order partial derivative matrices of the shape function are expressed as:

$$\begin{aligned} [B(s)] &= \begin{bmatrix} 0 & B_1(s) & B_4(s) & 0 & 0 & B_5(s) & B_8(s) & 0 \\ B_1(s) & 0 & 0 & B_4(s) & B_5(s) & 0 & 0 & B_8(s) \end{bmatrix}, \\ [R(s)] &= \begin{bmatrix} R_1(s) & 0 & 0 & R_4(s) & R_5(s) & 0 & 0 & R_8(s) \\ 0 & R_1(s) & R_4(s) & 0 & 0 & R_5(s) & R_8(s) & 0 \end{bmatrix}. \end{aligned} \tag{6}$$

2.2. Energy equation of thermal element

For a high-speed rotor operating at normal temperature, the formulas of kinetic energy and mechanical potential energy are widely applied [6]. The kinetic energy of the rotating beam element is composed of rotational kinetic energy and translational energy, expressible as:

$$KE = \frac{1}{2}\int_0^{l_s} \{\rho_s A_s(\dot{x}_a^2 + \dot{y}_a^2) + J_{ps}\Omega(\dot{\theta}_a\varphi_a - \theta_a\dot{\varphi}_a) + J_{ds}(\dot{\theta}_a^2 + \dot{\varphi}_a^2) + J_{ps}\Omega^2\}\mathrm{d}z, \tag{7}$$

where ρ_s, A_s, J_{ds} and J_{ps} represent the density, cross-sectional area, diametral and polar moments of inertia for the rotor element, respectively. Considering the influences of both bending and shearing, the mechanical potential energy of the rotor element under room temperature conditions is formulated as:

$$U^M = \frac{1}{2}\int_0^{l_s} E_s I_s \left[\left(\frac{\partial\theta_a}{\partial s}\right)^2 + \left(\frac{\partial\varphi_a}{\partial s}\right)^2\right]ds + \frac{1}{2}\int_0^{l_s} K_s^{'} G_s A_s\left[\left(\frac{\partial x_a}{\partial s} - \varphi_a\right)^2 + \left(\frac{\partial y_a}{\partial s} + \theta_a\right)^2\right]ds, \tag{8}$$

where E_s, G_s, I_s and K_s' represent the elastic modulus, shear modulus, area moment of inertia, and shear coefficient of the thermal rotor element, respectively.

In a high-temperature operating environment, the flexible rotor undergoes temperature-induced expansion or contraction deformations. When the rotating rotor is subject to external constraints or exhibits mutual constraints among its internal components, the flexible element experiences temperature-induced stresses. Consequently, the total potential energy U of the thermal rotor element consists of thermal potential energy U^T and mechanical potential energy U^M.

$$U = U^T + U^M. \tag{9}$$

In conformity with elasticity theory, the thermal potential energy U^T emerges as a composite of normal and shear strain energies. Assuming isotropy in the rotor material, signifying shear strain energy $U_\gamma^T = 0$, the resulting expression for thermal potential energy is articulated as:

$$U^T = \frac{1}{2}\iiint_V \sigma_z^{Temp}\varepsilon_z dV. \tag{10}$$

For delineating the connection between strain and displacement, the axial strain can be derived utilizing the von Karman nonlinear theory and elasticity theory.

$$\varepsilon_z = \frac{\partial u_z}{\partial s} + \frac{1}{2}\left(\frac{\partial u_y}{\partial s}\right)^2 + \frac{1}{2}\left(\frac{\partial u_x}{\partial s}\right)^2 - \varepsilon_z^T = \frac{\partial z_a}{\partial s} - x\frac{\partial\varphi_a}{\partial s} - y\frac{\partial\theta_a}{\partial s} + \frac{1}{2}\left(\frac{\partial x_a}{\partial s}\right)^2 + \frac{1}{2}\left(\frac{\partial y_a}{\partial s}\right)^2 - \varepsilon_z^T, \tag{11}$$

where ε_z^T is the strain caused by temperature difference. The association between linear displacement and angular displacement can be approximated as:

$$\varphi_a = \frac{\partial x_a}{\partial s},\ \theta_a = \frac{\partial y_a}{\partial s}. \tag{12}$$

Therefore, the axial strain is articulated as follows:

$$\varepsilon_z = \frac{\partial z_a}{\partial s} - x\frac{\partial\varphi_a}{\partial s} + y\frac{\partial\theta_a}{\partial s} + \frac{1}{2}{\theta_a}^2 + \frac{1}{2}{\varphi_a}^2 - \varepsilon_z^T. \tag{13}$$

Following the principles of elastic mechanics, the expression for axial thermal stress in both an infinitely long cylinder (Fig. 2(a)) and a finitely long cylinder with fully axially constrained ends (Fig. 2(b)) is as follows:

$$\sigma_z^{Temp}(i) = \frac{2\mu_s E_s\alpha_s}{(1-\mu_s)(r_o^2 - r_i^2)}\int_{r_i}^{r_o}\rho T(\rho, z_i)d\rho - \frac{E_s\alpha_s T(\rho, z_i)}{1-\mu_s}, \tag{14}$$

where μ_s, α_s, r_o and r_i represent the Poisson's ratio, thermal expansion coefficient, outer diameter and inner diameter of the thermal rotor element, respectively. The axial thermal stress in a cylinder of finite length, devoid of axial constraints (Fig. 2(c)), is denoted as:

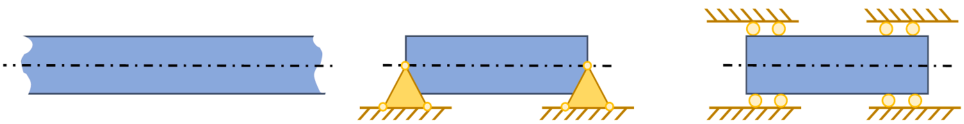

Fig. 2. The axial restraint state of thermal rotor.

$$\sigma_z^{Temp}(i) = \frac{2E_s\alpha_s}{(1-\mu_s)\left(r_o^2 - r_i^2\right)}\int_{r_i}^{r_o}\rho T(\rho)d\rho - \frac{E_s\alpha_s T(\rho)}{1-\mu_s}. \tag{15}$$

Per Hooke's law, a linear proportional relationship exists between stress and strain within a specific range, expressed as $\varepsilon_z^T = \sigma_z^{Temp}/E_s$. Substituting the axial strain and the axial thermal stress into Eq. (10), the thermal potential energy can be obtained as:

$$\begin{aligned} U^T = & \frac{1}{2}\int_0^{l_s}\left[\int_A \sigma_z^{Temp}dA\right]\left[\frac{1}{2}\theta_a^2 + \frac{1}{2}\varphi_a^2\right]ds - \frac{1}{2}\int_0^{l_s}\left[\int_A \sigma_z^{Temp}xdA\right]\frac{\partial\varphi_a}{\partial s}ds \\ & + \frac{1}{2}\int_0^{l_s}\left[\int_A \sigma_z^{Temp}ydA\right]\frac{\partial\theta_a}{\partial s}ds + \frac{1}{2}\int_0^{l_s}\left[\int_A \sigma_z^{Temp}dA\right]\frac{\partial z_a}{\partial s}ds - \frac{1}{2}\iiint_V \left(\sigma_z^{Temp}\right)^2 \Big/ E_s dV. \end{aligned} \tag{16}$$

The core tenet of the finite element method lies in the discretization of continuous systems. Diverse thermal rotor elements exhibit distinct thermal stress $\sigma_z^{Temp}(i)$, as shown in Fig. 3, yet each can be deemed to possess a uniform thermal stress expression along any section in the axial direction.

Consequently, the integration of thermal stress at any section for a thermal rotor element is used to calculate the section's normal force and bending moment resulting from the thermal stress of each element.

$$\begin{aligned} N^T &= \int_A \sigma_z^{Temp}dA, \\ M_x^T &= \int_A \sigma_z^{Temp}xdA, \\ M_y^T &= \int_A \sigma_z^{Temp}ydA. \end{aligned} \tag{17}$$

Substituting Eq. (17) into Eq. (16), the thermal potential energy is obtained:

$$\begin{aligned} U^T = U_1^T + U_2^T + U_3^T + U_4^T + U_5^T = & \frac{1}{4}N^T\int_0^{l_s}\left[\theta_a^2 + \varphi_a^2\right]ds - \frac{1}{2}M_x^T\int_0^{l_s}\frac{\partial\varphi_a}{\partial s}ds \\ & + \frac{1}{2}M_y^T\int_0^{l_s}\frac{\partial\theta_a}{\partial s}ds + \frac{1}{2}N^T\int_0^{l_s}\frac{\partial z_a}{\partial s}ds - \frac{1}{2}\iiint_V \left(\sigma_z^{Temp}\right)^2 \Big/ E_s dV. \end{aligned} \tag{18}$$

Substituting the displacement and angle Eqs. (3)–(6) of any point on the centroid axis into the thermal energy Eq. (18), the thermal potential energy decomposed into five parts can be expressed as:

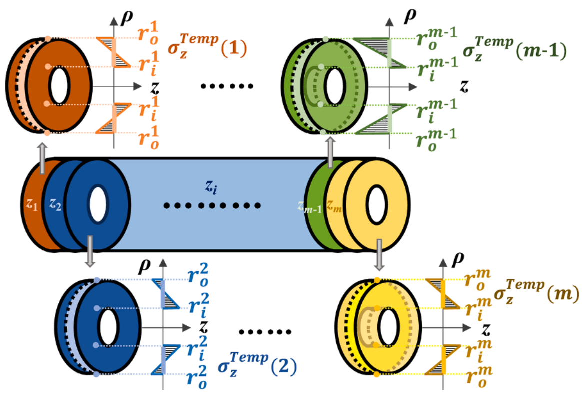

Fig. 3. The thermal stress of discrete thermal rotor element.

$$
\begin{aligned}
U_1^T &= \frac{1}{4}N^T \int_0^{l_s} \left[\begin{array}{l} (-D_1(s)y_1 + D_4(s)\theta_1 - D_5(s)y_2 + D_8(s)\theta_2)^2 \\ +(D_1(s)x_1 + D_4(s)\varphi_1 + D_5(s)x_2 + D_8(s)\varphi_2)^2 \end{array} \right] ds, \\
U_2^T &= -\frac{1}{2}M_x^T \int_0^{l_s} (R_1x_1 + R_4\varphi_1 + R_5x_2 + R_8\varphi_2)ds, \\
U_3^T &= \frac{1}{2}M_y^T \int_0^{l_s} (-R_1y_1 + R_4\theta_1 - R_5y_2 + R_8\theta_2)ds, \\
U_4^T &= 0, \\
U_5^T &= 0.
\end{aligned} \tag{19}
$$

2.3. Temperature-dependent material property

Acknowledging the temperature dependence of materials, common structural metals exhibit expressible properties correlating with temperature [42]:

$$
\Gamma = \Gamma_0(\Gamma_{-1}T^{-1} + \Gamma_0 + \Gamma_1 T + \Gamma_2 T^2 + \Gamma_3 T^3), \tag{20}
$$

where Γ represents temperature-dependent parameters of the material, including the elastic modulus, shear modulus, Poisson's ratio, and others. Γ_{-1},Γ_0,Γ_1,Γ_2,Γ_3 are coefficients of the temperature-dependent material property function. The complexity of material performance under varying temperature conditions is acknowledged. This research employs 45 steel for a comprehensive series of numerical analyses. Fig. 4 illustrates the variations in material parameters with temperature.

2.4. Equations of motion

The Lagrange equation is expressed as:

$$
\frac{\partial}{\partial t}\left(\frac{\partial KE}{\partial \dot{q}_i}\right) - \frac{\partial KE}{\partial q_i} + \frac{\partial U^M}{\partial q_i} + \frac{\partial U^T}{\partial q_i} = 0, i = 1, 2, \ldots. \tag{21}
$$

In response to temperature-induced potential energy in the flexible rotor, the decomposed thermal potential energy Eq. (19) is substituted into Eq. (21). By calculating the partial derivatives of thermal potential energy, the expressions for $U_1^T/\partial q_i$, $U_2^T/\partial q_i$, and $U_3^T/\partial q_i$ are derived (detailed expressions are provided in the Appendix A). Similarly, the kinetic energy Eq. (7) and mechanical potential energy Eq. (8) are substituted into the Lagrange Eq. (21). The dynamic equation of the thermal rotor element in matrix notation is as follows:

$$
[M]^e\{\ddot{q}\}_s + [C]^e\{\dot{q}\}_s + \Omega[G]^e\{\dot{q}\}_s + [K]_M^e\{q\}_s + [K]_T^e\{q\}_s + [K]_b^e\{q\}_s = [f]_{unl}^e, \tag{22}
$$

where $[K]_T^e$ denotes the temperature stiffness matrix (the matrix is shown in Appendix A), employed to characterize the influence of temperature stress. The matrices $[M]^e$, $[C]^e$, $[G]^e$, $[K]_M^e$, $[K]_b^e$, $[f]_{unl}^e$ correspondingly signify the mass matrix, damping matrix, gyro matrix, mechanical stiffness matrix, bearing stiffness, and unbalanced force vector of the thermal rotor element (refer to the literature [43] for detailed information). In accordance with the finite element assembly method, the dynamic equation of the thermal rotor is established as follows:

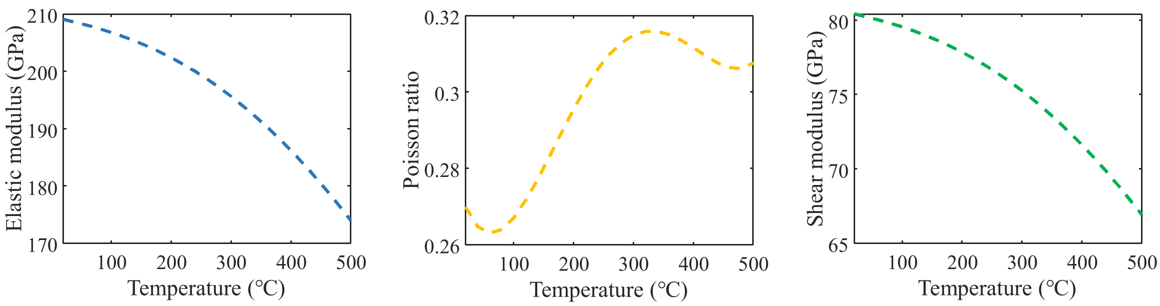

(a) Elastic modulus (b) Poisson's ratio (c) Shear modulus

Fig. 4. Material properties of 45 steel with temperature.

$$[M]\{\ddot{q}\} + [C]\{\dot{q}\} + \Omega[G]\{\dot{q}\} + [K]_M\{q\} + [K]_T\{q\} + [K]_b\{q\} = [f]_{unl}, \tag{23}$$

where $[M]$, $[C]$, $[G]$, $[K]_M$, $[K]_T$, $[K]_b$, $[f]_{unl}$ are the mass matrix, damping matrix, gyro matrix, mechanical stiffness matrix, thermal stiffness matrix, bearing stiffness and unbalanced force vector of the thermal rotor structure, respectively. $\{q\}$ is the generalized vector of the thermal rotor, expressed as:

$$\{q\} = [x_1, y_1, \theta_1, \varphi_1, x_2, y_2, \theta_2, \varphi_2, \ldots\ldots, x_{m-1}, y_{m-1}, \theta_{m-1}, \varphi_{m-1}, x_m, y_m, \theta_m, \varphi_m]^T. \tag{24}$$

3. Temperature field model

The heat transfer partial differential equation for an axisymmetric structure, taking into account internal heat sources and the transient temperature field, is expressed as [44]:

$$\frac{\partial T}{\partial t} = \frac{k}{c_p \rho_s}\left(\frac{\partial^2 T}{\partial r^2} + \frac{1}{r}\frac{\partial T}{\partial r} + \frac{\partial^2 T}{\partial z^2} + \frac{q_v}{k}\right), \tag{25}$$

where k denotes thermal conductivity, q_v represents internal heat source, c_p signifies the specific heat at constant pressure, t signifies time, and z and r denote the axial and radial coordinates of the axisymmetric structure, respectively. The derivation of the weighted residual formula is grounded in the Galerkin method. Subsequently, the variational equation for the axisymmetric temperature field is obtained through partial integration and Green's formula.

$$\begin{aligned}\frac{\partial J^D}{\partial T_l} = &\iint_D \left[kr\left(\frac{\partial W_l}{\partial r}\frac{\partial T}{\partial r} + \frac{\partial W_l}{\partial z}\frac{\partial T}{\partial z}\right) - W_l r q_v + W_l r \rho c_p \frac{\partial T}{\partial t}\right] dzdr \\ &- \oint_\Gamma W_l rk \frac{\partial T}{\partial n} ds = 0, \ (l = 1, 2, \ldots, n).\end{aligned} \tag{26}$$

Building upon the temperature field boundary conditions, the variational calculation equations for the axisymmetric temperature field are derived. The first boundary conditions encompass three cases: defining the boundary ij as temperature T, adiabatic or internal heat conduction (Fig. 5). The variational expression for the first boundary conditions element is explicitly formulated in Eq. (27). As shown in Fig. 5, the second and third boundaries respectively define the heat flux q_2 and convective heat transfer (convection heat transfer coefficient h and medium temperature T_3) of the boundary ij. Their variational formulas are presented as Eqs. (28) and (29).

$$\frac{\partial J^E}{\partial T_l} = \iint_E \left[kr\left(\frac{\partial W_l}{\partial r}\frac{\partial T}{\partial r} + \frac{\partial W_l}{\partial z}\frac{\partial T}{\partial z}\right) - W_l r q_v + W_l r \rho c_p \frac{\partial T}{\partial t}\right] dzdr, \tag{27}$$

$$\frac{\partial J^E}{\partial T_l} = \iint_E \left[kr\left(\frac{\partial W_l}{\partial r}\frac{\partial T}{\partial r} + \frac{\partial W_l}{\partial z}\frac{\partial T}{\partial z}\right) - W_l r q_v + W_l r \rho c_p \frac{\partial T}{\partial t}\right] dzdr - \int_{ij} W_l r q_2 ds, \tag{28}$$

$$\frac{\partial J^E}{\partial T_l} = \iint_E \left[kr\left(\frac{\partial W_l}{\partial r}\frac{\partial T}{\partial r} + \frac{\partial W_l}{\partial z}\frac{\partial T}{\partial z}\right) - W_l r q_v + W_l r \rho c_p \frac{\partial T}{\partial t}\right] dzdr - \int_{ij} W_l r \alpha_s (T - T_3) ds, \tag{29}$$

where E signifies a finite element domain of the axisymmetric structure, and$l = (i, j, m)$ constitutes an array of nodes for an element. The temperature of any point in an element can be expressed by temperature shape function of temperature $[H]^e$ and the temperature of nodes:

$$T = [H]^e [T_i,\ T_j,\ T_m]^{\mathrm{T}} = [H_i,\ H_j,\ H_m][T_i,\ T_j,\ T_m]^{\mathrm{T}}. \tag{30}$$

The weight function of node is

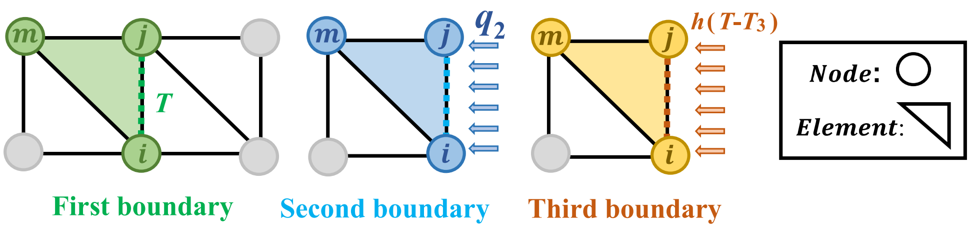

Fig. 5. Three types of boundaries.

$$W_l = \frac{\partial T}{\partial T_l} = H_l, l = (i,\ j,\ m). \tag{31}$$

The temperature shape function (Eq. (30)) and the weight function (Eq. (31)) are substituted into the variational formulas (Eqs. (27)-(29)). Upon organizing the variational formula for the element, the temperature field of the finite element is subsequently derived.

$$[KT]^E\{T\}^E + [NT]^E\left\{\frac{\partial T}{\partial t}\right\}^E = \{PT\}^E, \tag{32}$$

where $\{T\}^E$ denotes the element temperature vector, while $[KT]^E$, $[NT]^E$, and $\{PT\}^E$ stand for the element thermal conductivity matrix, element heat capacity matrix, and temperature load vector, respectively. The overall temperature field model is determined by the characteristics of the specific temperature solution domain and the distribution of element nodes.

4. Numerical results

Building upon the Sections 2 and 3, this section presents the numerical analysis results. Detailed descriptions of temperature boundary conditions for the subsequent numerical analysis are provided. The effects of thermal stress, temperature-dependent material properties, and coupling effect on the vibration response of the thermal rotor under various temperature fields are discussed individually.

To investigate the vibration characteristics of the thermal rotor, subsequent analysis is conducted for a rotor with both ends fully axially constrained, as illustrated in Fig. 6. Table 1 provides the geometry and material parameters of the thermal rotor.

4.1. Temperature distribution of rotor

Fig. 7 shows the boundary conditions of temperature field. These conditions are specified as follows:

Surface 1 and Surface 5 are adiabatic;

Surface 2 and Surface 4 experience convective heat transfer with room temperature air at 22 °C, with a convective heat transfer coefficient of 40 W/(m^2·K);

Surface 3 undergoes convective heat transfer with high temperature gas at $\Delta T + 22$ °C, with a convective heat transfer coefficient of 60 W/(m^2·K).

In this study, the room temperature is assumed to be 22 °C (temperature difference ΔT=0 °C), as portrayed in the upper part of Fig. 8(a). Similarly, when high-temperature gas T_3=72 °C or 122 °C, the temperature difference ΔT is 50 °C or 100 °C, respectively. Employing the temperature field model in Section 3 yields the temperature distribution results showcased in Fig. 8. The computed non-uniform temperature distribution results are substituted into the thermal stiffness matrix and temperature-dependent material parameters, enabling the analysis of the influence of varying boundary conditions on the vibration characteristics.

4.2. Analysis of NF characteristics

4.2.1. The influence of axial thermal stress on the NF

Fig. 9 illustrates the axial thermal stress distribution of the thermal rotor under various temperature boundary conditions. The thermal stress distribution in the rotor closely resembles the temperature distribution. Furthermore, the maximum axial thermal stress undergoes a proportional increase as the temperature difference grows.

Fig. 10 displays the first- to fourth-order NFs of the thermal rotor under various temperature distributions, considering the impact of thermal stress. The lower left corner depicts the mode shape, while the upper right corner showcases the NF's difference. As the temperature difference ΔT increases from 0 °C to 150 °C, the first-order NF decreases by 11.6 Hz, the second-order NF decreases by 20.1 Hz, the third-order NF decreases by 16.9 Hz, and the fourth-order NF decreases by 15.1 Hz. The investigation of the NF variations

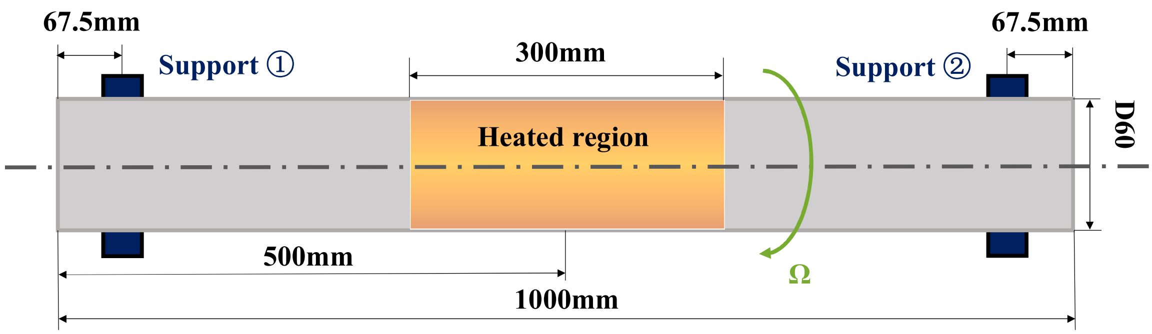

Fig. 6. The schematic diagram of thermal rotor.

Table 1
The geometry and material parameters of thermal rotor (Normal temperature).

Geometry parameters	Value	Material parameters	Value
Beam length	1000 mm	Elastic modulus E_s	209 GPa
Beam diameter	60 mm	Poisson's ratio ν_s	0.3
Heated region position	500 mm	Density ρ_s	7890 kg/m^3
Heated region range	300 mm	Shear modulus G_s	80.4 GPa
Support① position	67.5 mm	Thermal expansion coefficient α_s	1.2×10^{6} °C^{-1}
Support② position	932.5 mm	Support stiffness	1×10^{11} N/mm

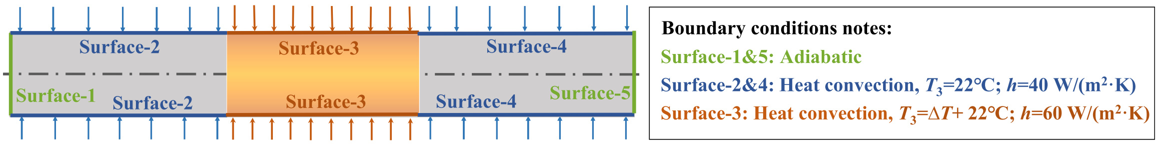

Fig. 7. The boundary conditions of temperature field.

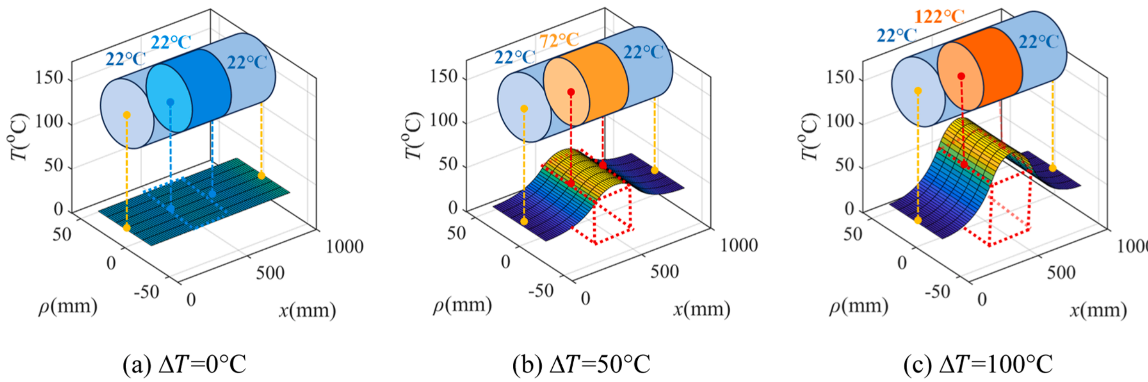

Fig. 8. The temperature field distribution.

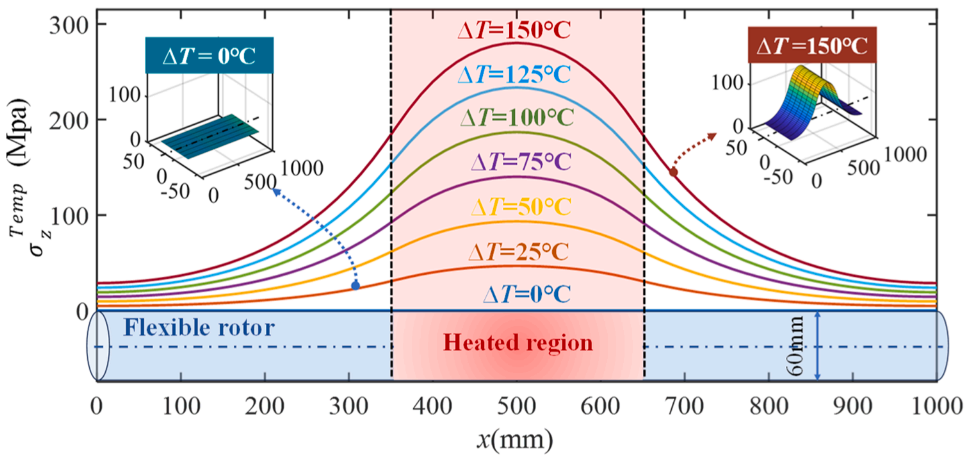

Fig. 9. The axial thermal stress distribution.

induced by axial thermal stress reveals that the second-order NF experiences the most significant variation with temperature difference.

4.2.2. The influence of temperature-dependent material properties on the NF

Fig. 11 presents the variation of the first- to fourth-order NFs under various temperature field conditions, taking into account the

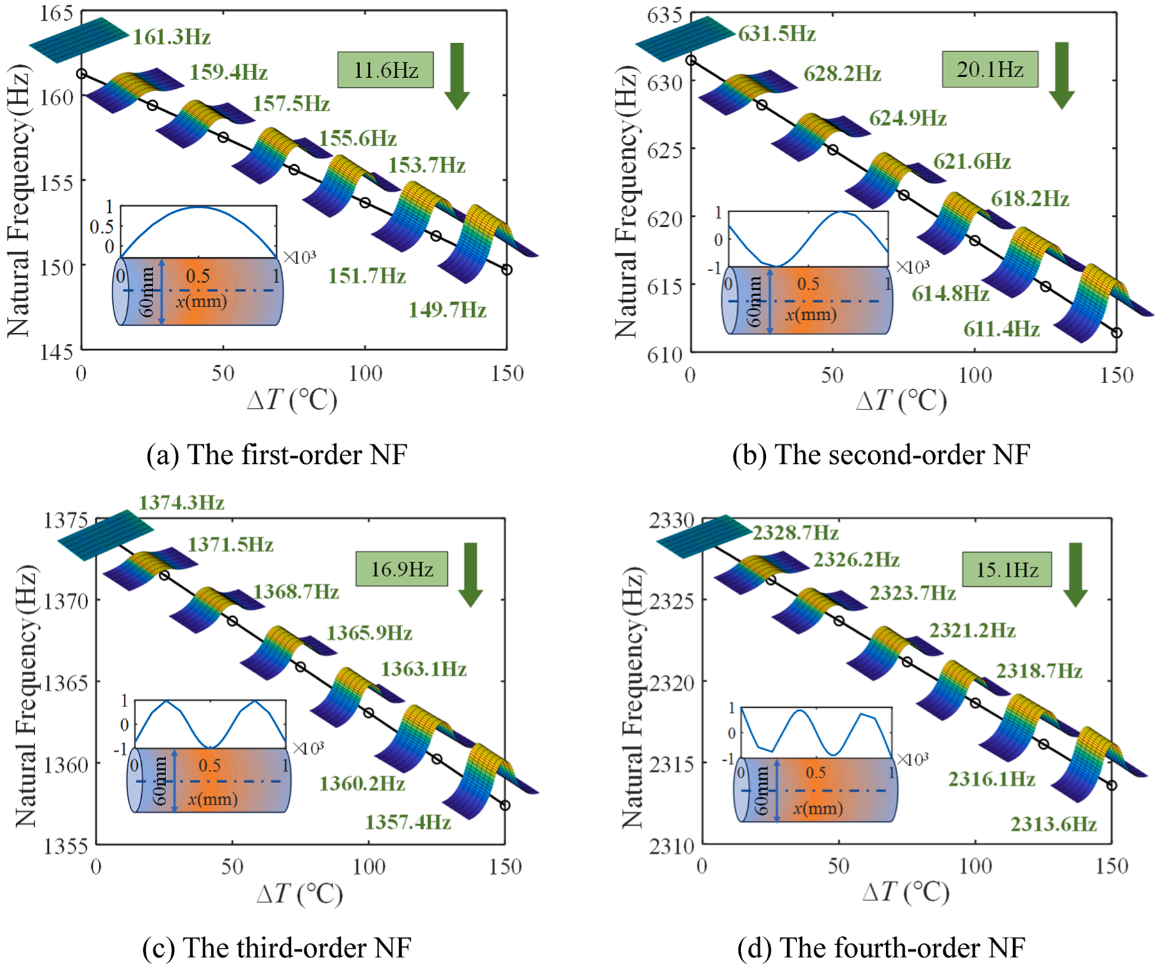

(a) The first-order NF

(b) The second-order NF

(c) The third-order NF

(d) The fourth-order NF

Fig. 10. The NF variations induced by axial thermal stress.

influence of temperature-dependent material properties. As the temperature difference increases from 0 °C to 150 °C, the first-order NF experiences a reduction of 2.0 Hz, and the second-order NF decreases by 7.9 Hz, and the third-order NF decreases by 17.1 Hz, and the fourth-order NF decreases by 29.0 Hz. Notably, a discernible trend emerges: higher order NFs exhibit more substantial decreases in NFs with increasing temperature difference.

4.2.3. The coupling influence of axial thermal stress and material properties on the NF

Fig. 12 illustrates the variation in the first- to fourth-order NFs under diverse temperature field distributions. This analysis comprehensively incorporates the coupling influence of axial thermal stress and temperature-dependent material properties. As the temperature difference escalates from 0 °C to 150 °C, the first to fourth-order NFs experience reductions of 13.5 Hz, 27.7 Hz, 33.8 Hz, and 43.9 Hz, respectively. Notably, the relationship persists that higher order NFs show more pronounced decreases in NFs with increasing temperature difference.

4.3. Analysis of dimensionless natural frequency (DNF) characteristics

To objectively assess the impact of various factors and ensure the generality of numerical outcomes, this section concentrates on elucidating the changes in DNFs arising from axial thermal stress, temperature-dependent material parameters, and their coupling effect.

Fig. 13 illustrates the alteration in DNFs with temperature resulting from axial thermal stress. Despite Fig. 13 revealing the smallest difference in first-order NF under the same temperature difference, dimensionless analysis demonstrates that axial thermal stress has the most significant impact on the first-order DNF. Conversely, its influence diminishes on higher-order DNFs.

Fig. 14 illustrates the variation in DNFs from the first- to fourth-order resulting from temperature-dependent material. As the temperature difference increases, the DNF of each order uniformly decreases. This observation underscores the consistent influence of temperature-dependent material on each DNF.

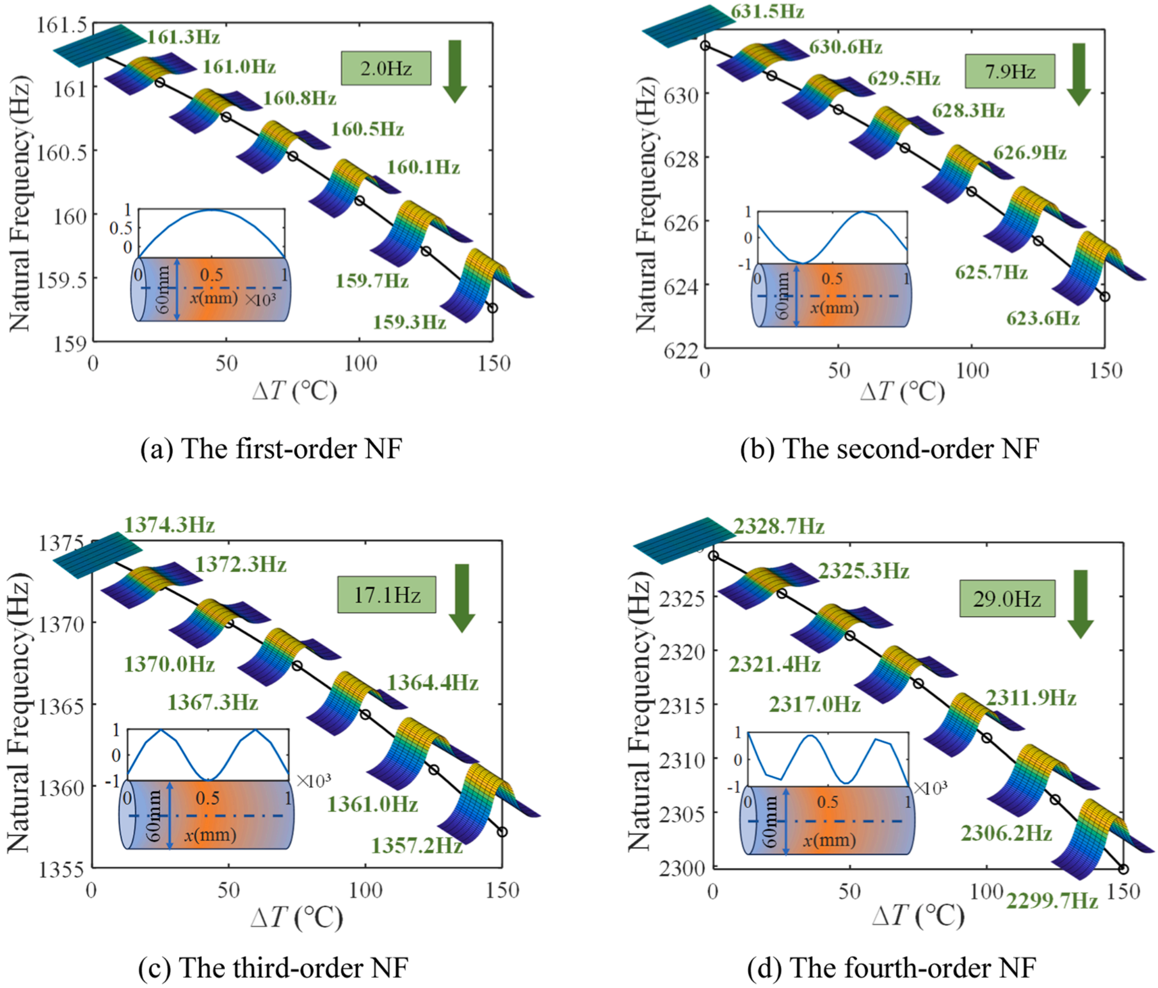

Fig. 11. The NF variations induced by material properties.

Fig. 15 illustrates the alteration in DNFs resulting from the synergistic interplay of axial thermal stress and temperature-dependent material properties. Within identical temperature differentials, the coupling effect exerts its most significant impact on the first-order DNF, with its influence intensifying progressively alongside escalating temperature variations.

4.4. Run-up response

In this section, the analysis focuses on the impact of axial thermal stress, temperature-dependent material properties, and coupling effect on the run-up response of the thermal rotor.

Fig. 16 elucidates the run-up response of a thermal rotor, accounting for axial thermal stress amidst diverse temperature differences. Fig. 16(a) specifically presents the rotor response as speed escalates from 0 to 18,000 rpm. Significantly, antecedent to the initiation of first-order resonance frequency, augmented temperature differences correlate positively with heightened response amplitudes. Conversely, subsequent to the onset of first-order resonance frequency, augmented temperature differences yield a proportional reduction in the amplitude of the thermal rotor. Fig. 16(b) illustrates the response as the rotating speed elevates from 30,000 to 42,000 rpm. This analysis is instrumental in scrutinizing the influence of temperature on the response proximate to the second-order resonance frequency. Antecedent to the initiation of second-order resonance frequency, heightened temperatures correspond with a diminished amplitude of the thermal rotor. At the resonance point, akin to the first-order resonance frequency, escalating temperature differences lead to a reduction in the second-order resonance frequency value. However, distinct from the first-order resonance frequency, at the second-order resonance point, an augmented temperature difference results in an amplified amplitude. Subsequent to the occurrence of second-order resonance frequency, the amplitude diminishes with rising temperature, mirroring the phenomenon observed prior to the onset of second-order resonance frequency.

Fig. 17 presents the run-up response under varied temperature differences, incorporating the impact of temperature-changing material properties. Within the rotating speed range of 0–18,000 rpm and 30,000–42,000 rpm, the observed phenomenon mirrors

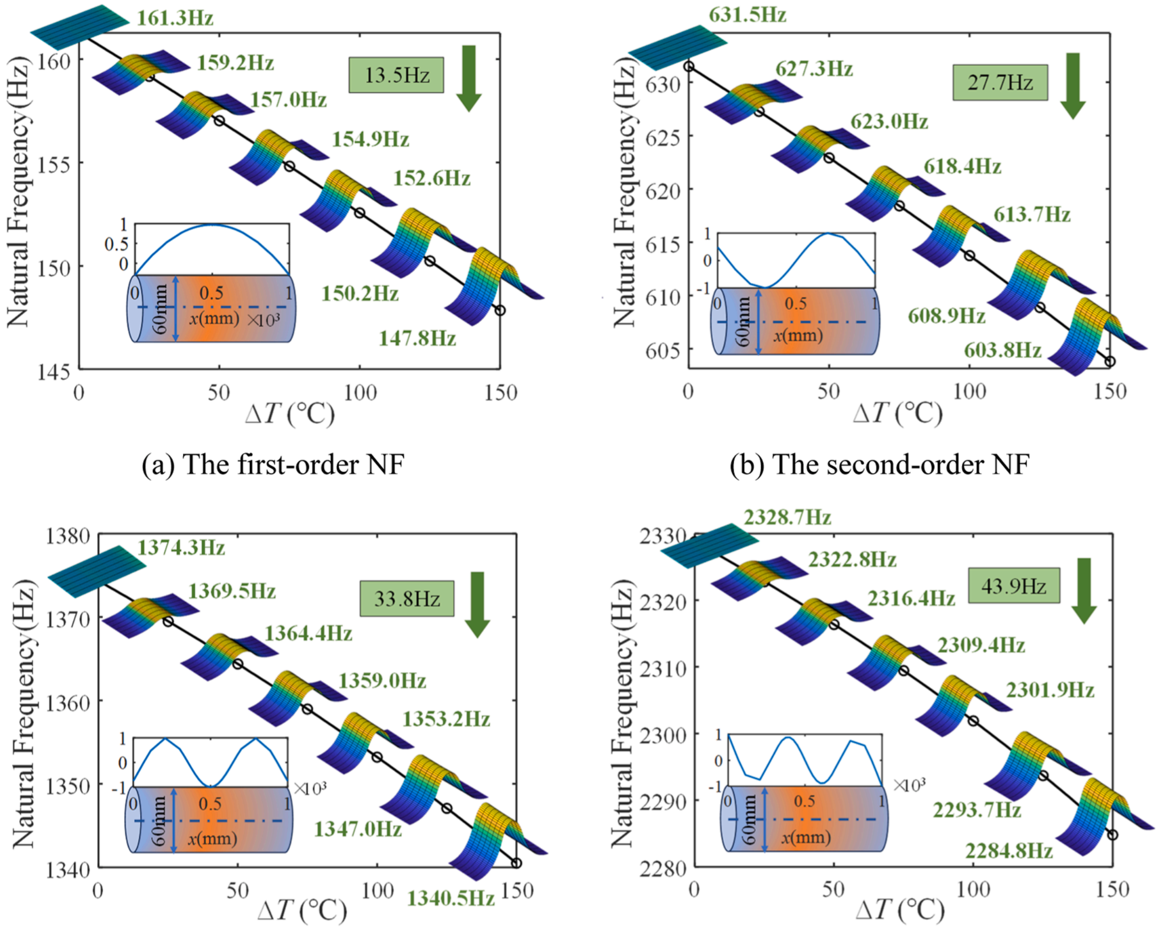

(a) The first-order NF (b) The second-order NF

(c) The third-order NF (d) The fourth-order NF

Fig. 12. The NF variations induced by coupling effect.

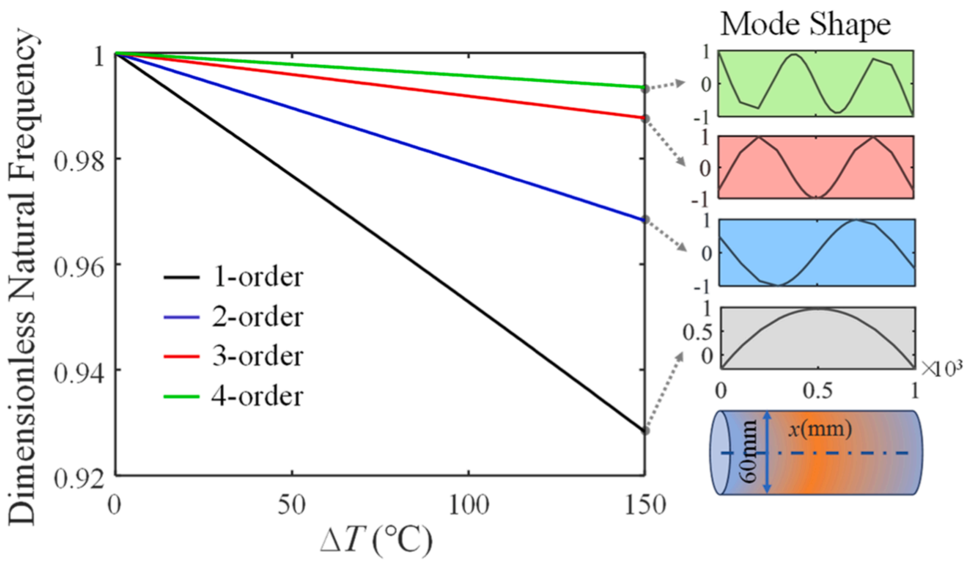

Fig. 13. The DNF changes induced by axial thermal stress.

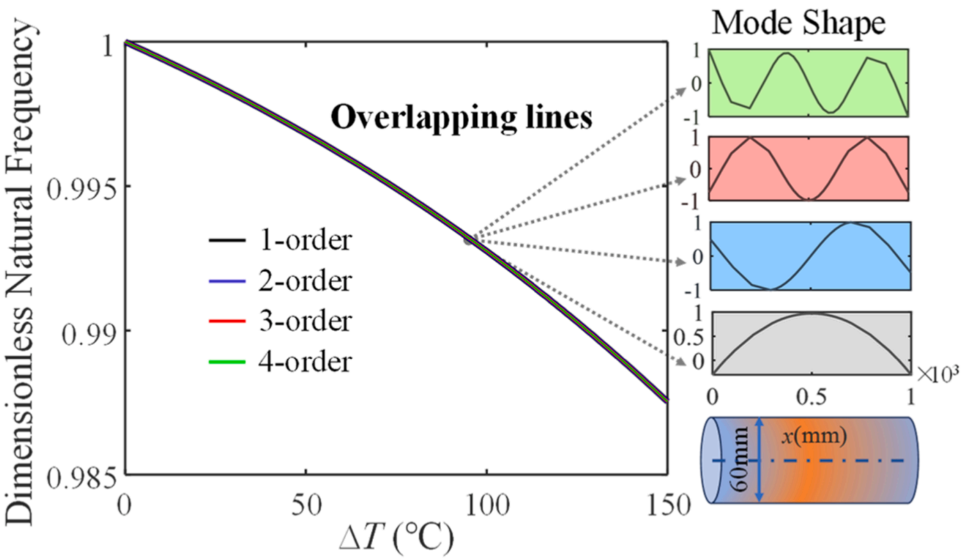

Fig. 14. The DNF changes induced by temperature-dependent materials.

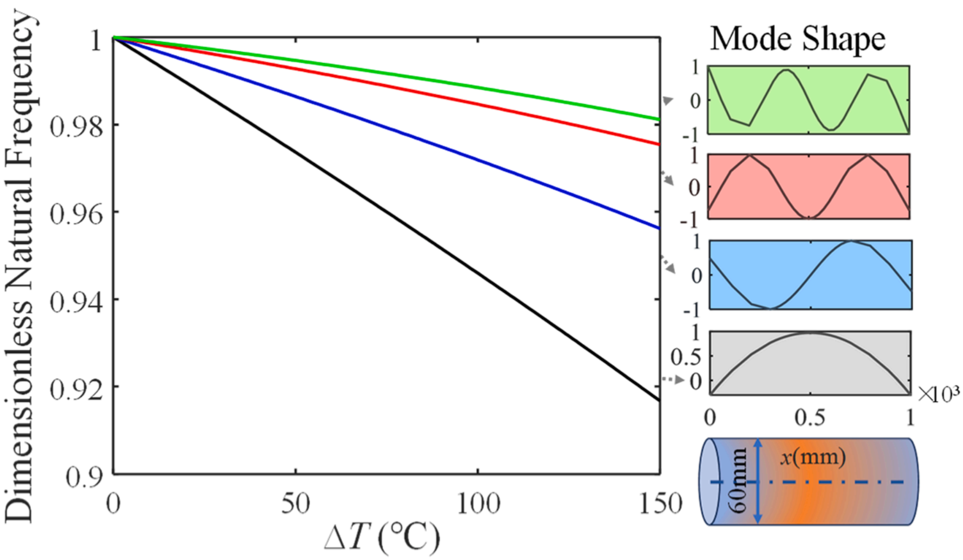

Fig. 15. The DNF changes induced by coupling effect.

the influence of thermal stress. Notably, in contrast to axial thermal stress, the effect of temperature-dependent material properties on the amplitude of the run-up response is exceedingly nuanced.

Fig. 18 illustrates alterations in the run-up response under varying temperature differences, incorporating the coupling effect of axial thermal stress and temperature-dependent material properties. Despite the distinct impact degree of axial thermal stress and temperature-dependent material properties on the run-up response, their influence exhibits consistent trends. Consequently, the impact of coupling becomes increasingly evident, resulting in conspicuous changes in frequency and amplitude with the escalation of temperature differences.

5. Model validation

Section 5 is dedicated to validating the proposed one-dimensional model, which incorporates considerations of axial thermal stress and temperature-dependent material properties. The verification method employs a three-dimensional finite element model. The reliability of this verification method comes from dividing the rotor into many nodes and elements in three-dimensional space, which can accurately describe the thermal stress and strain at each location in the non-uniform temperature field. The rotor's vibration

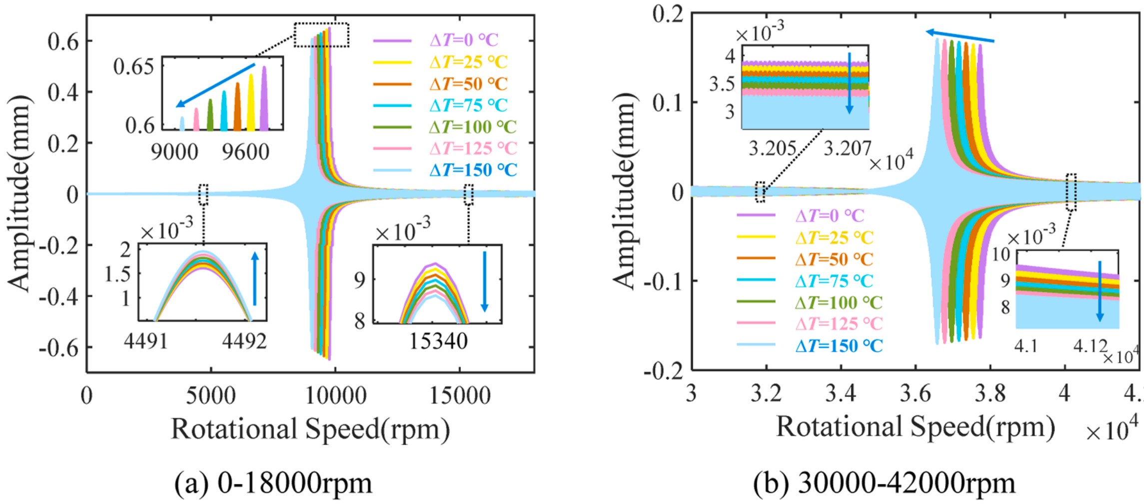

Fig. 16. The run-up response of thermal rotor induced by axial thermal stress.

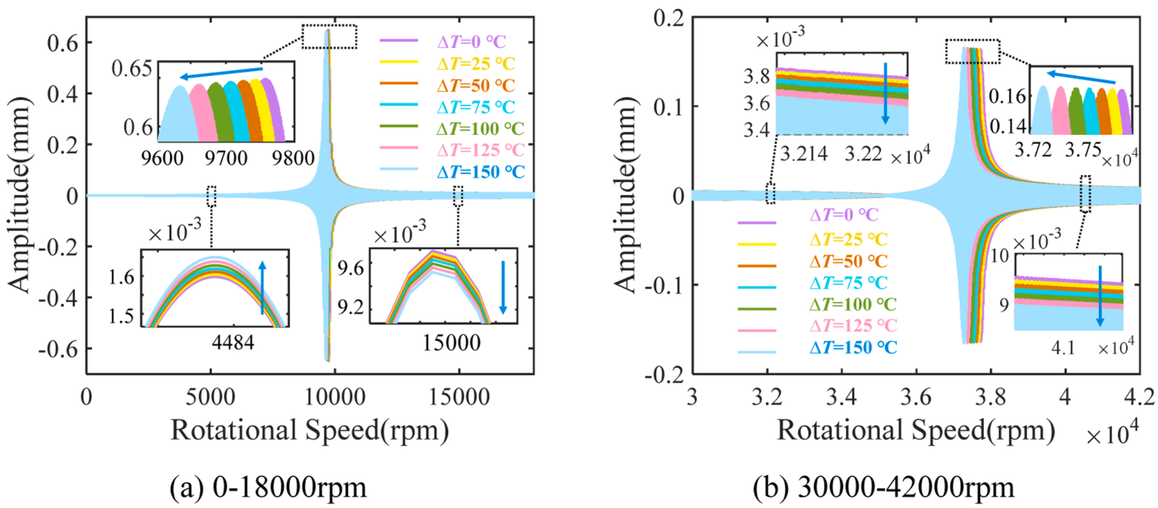

Fig. 17. The run-up response induced by temperature-dependent material properties.

characteristics are analyzed using this verification method, and the simulation outcomes are juxtaposed with the proposed model's analysis results. Fig. 19 illustrates the boundary conditions and the calculation results of the temperature distribution for the thermal rotor employed in the verification process.

Table 2 delineates the first-order NF of the thermal rotor, accounting for the influence of axial thermal stress, computed through the finite element method and the proposed model. Observation reveals that the discrepancy remains below 0.6 % for each temperature boundary condition.

Table 3 delineates the first-order NF of the thermal rotor, taking into account the coupling effect of axial thermal stress and temperature-dependent material properties, computed through the finite element method and the proposed model. Notably, for each temperature boundary condition, the discrepancy is observed to be <0.2 %. This affirms the efficacy of the model introduced in this study.

Fig. 20 shows the frequency error analysis considering axial thermal stress and coupling effect. The error considering coupling effect is significantly smaller than that considering only axial thermal stress.

6. Conclusions

In this paper, an accurate and simple thermal flexible rotor dynamic model is proposed, which accounts for the impact of thermal stress and temperature-dependent material properties on a flexible structure subjected to a non-uniform temperature field. Subsequently, the influence of multiple factors on thermoelastic coupling vibration characteristics (NF, DNF, and run-up response) under

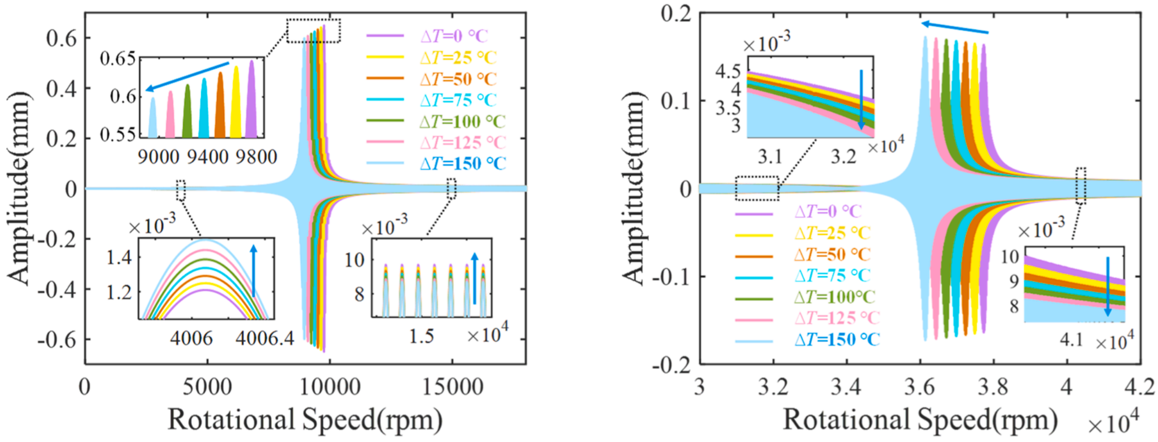

(a) 0-18000rpm (b) 30000-42000rpm

Fig. 18. The run-up response induced by the coupling effect.

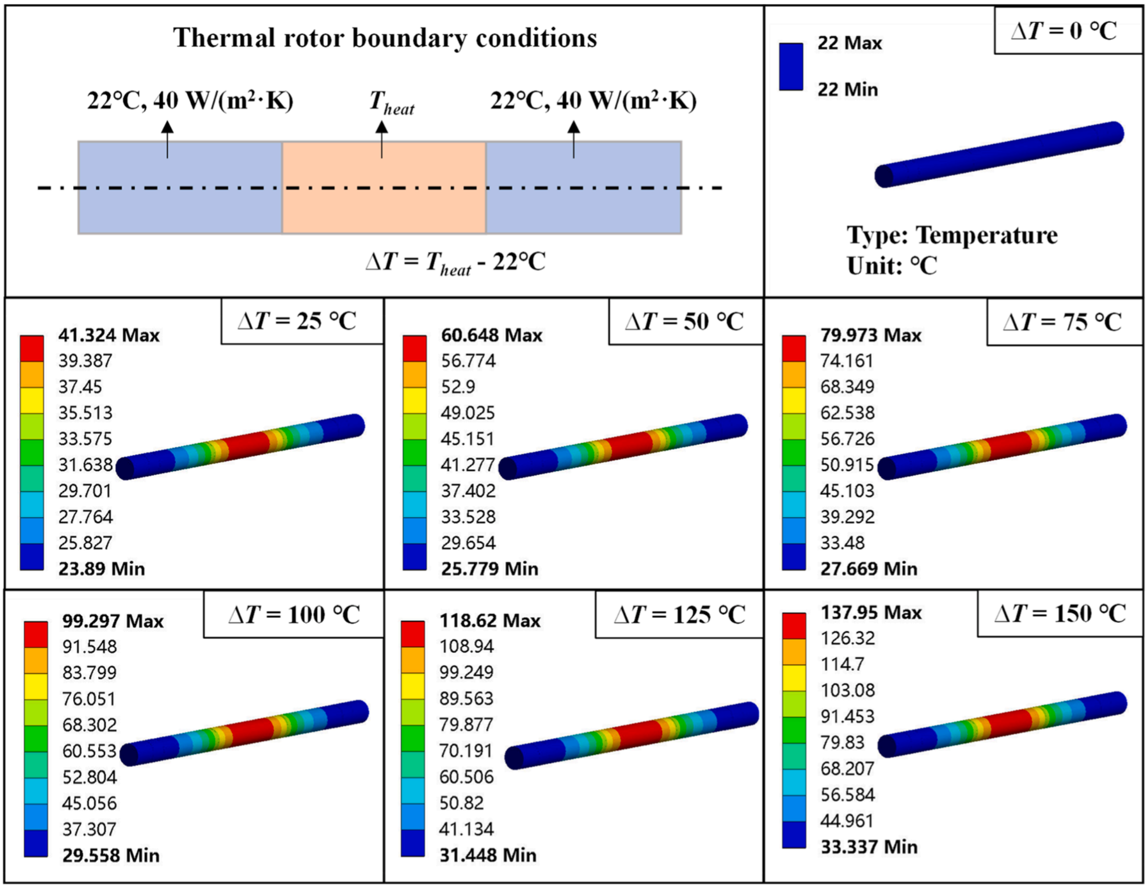

Fig. 19. Temperature boundary conditions and the calculation results using finite element software.

different temperature fields are discussed. Concurrently, the model's validity is confirmed through the three-dimensional finite element method. This model guarantees precise and simple characterization of temperature effects on the rotor, providing a rapid calculation model suitable for iterative and nonlinear analyses of thermal rotors.

Table 2
The first-order NF variations induced by axial thermal stress.

Temperature difference (°C)	FE model's NF (Hz)	The proposed model's NF (Hz)	Error (%)
0	161.2	161.3	0.06
25	159.3	159.4	0.06
50	157.3	157.5	0.12
75	155.3	155.6	0.19
100	153.2	153.7	0.31
125	151.0	151.7	0.43
150	148.8	149.7	0.56

Table 3
The first-order NF variations induced by coupling effect.

Temperature difference (°C)	FE model's NF (Hz)	The proposed model's NF (Hz)	Error (%)
0	161.2	161.3	0.06
25	159.2	159.2	0.00
50	157.1	157.0	0.06
75	154.9	154.9	0.00
100	152.74	152.6	0.09
125	150.42	150.2	0.15
150	147.99	147.8	0.13

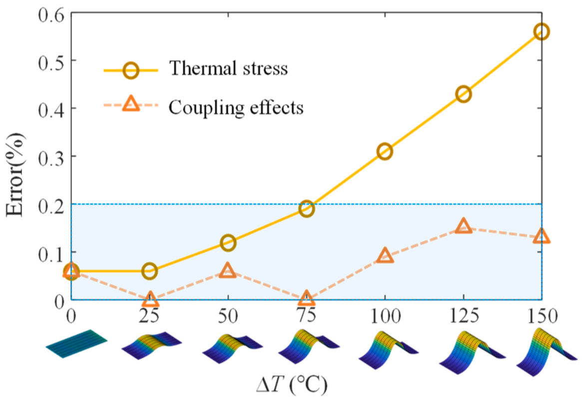

Fig. 20. The error analysis.

(1) A thermal flexible rotor modelling approach that incorporates considerations of thermal stress and temperature-dependent material properties is proposed to achieve rapid and precise computation of the thermal rotor response. Primarily, leveraging the shear deformation theory, the expression of deformation for an arbitrary point within the thermal rotor element is formulated through the coordinate of an arbitrary point along the element centroid line. Simultaneously, the coordinate of the arbitrary point on the centroid line is determined by the generalized coordinates of the element. Subsequently, the formula for strain concerning generalized coordinates is derived based on the von Karman strain–displacement relation. The theory of thermo-elasticity is employed to obtain the axial thermal stress of the thermal rotor element. By integrating the relationship between axial strain and thermal stress, the potential energy associated with thermal deformation is derived and subsequently incorporated into the Lagrange equation for assembly.
(2) The influences of thermal stress, temperature-dependent material properties, and the coupling effect on the NF, DNF, and run-up response of the thermal rotor under diverse temperature boundary conditions are examined. The NF is reduced by axial thermal stress, with the second-order NF exhibiting the most significant alterations. However, the DNF analysis reveals that temperature exerts the most substantial influence on low-order frequencies. Material properties also contribute to frequency reduction, yet the distinctive aspect is that the impact of material properties on each order DNF remains consistent. The run-up response analysis reveals that the amplitude is reduced by temperature stress, temperature-dependent material properties, and coupling effect across most speed ranges. This contrasts with the amplitude change induced by thermal bending. Consequently, comprehensive consideration of these temperature-induced effects is warranted when conducting thermoelastic coupling analysis.

(3) The validation of the model, incorporating the influences of thermal stress and temperature-dependent material properties, is conducted. To ensure consistency in temperature boundary conditions, a comparative analysis is undertaken between the calculation results of the proposed model and the three-dimensional finite element model. The analysis outcomes reveal that the NF error is maintained below 1 % under each temperature boundary condition.

CRediT authorship contribution statement

Yazheng Zhao: Writing – original draft, Validation, Data curation, Conceptualization. **Jin Zhou:** Writing – review & editing, Supervision, Funding acquisition. **Mingjie Guo:** Software, Data curation. **Yuanping Xu:** Writing – review & editing, Supervision.

Declaration of competing interest

The authors declare that they have no known competing financial interests or personal relationships that could have appeared to influence the work reported in this paper.

Acknowledgement

This work was supported by the National Natural Science Foundation of China [grant number 52075239].

Appendix A

The interpolation functions in the shape function matrix are expressed as:

$$\begin{aligned} N_1(s) &= \frac{1}{1+\lambda}\left(1+\lambda-\lambda\xi-3\xi^2+2\xi^3\right), \\ N_4(s) &= \frac{l_s}{1+\lambda}\left[\left(1+\frac{\lambda}{2}\right)\xi-\left(2+\frac{\lambda}{2}\right)\xi^2+\xi^3\right], \\ N_5(s) &= \frac{1}{1+\lambda}\left(\lambda\xi+3\xi^2-2\xi^3\right), \\ N_8(s) &= \frac{l_s}{1+\lambda}\left[-\frac{\lambda}{2}\xi+\left(\frac{\lambda-2}{2}\right)\xi^2+\xi^3\right]. \end{aligned} \tag{A.1}$$

$$\begin{aligned} D_1(s) &= \frac{6}{(1+\lambda)l_s}\left(-\xi+\xi^2\right), \\ D_4(s) &= \frac{1}{1+\lambda}\left(1+\lambda-(4+\lambda)\xi+3\xi^2\right), \\ D_5(s) &= \frac{6}{(1+\lambda)l_s}\left(\xi-\xi^2\right), \\ D_8(s) &= \frac{1}{1+\lambda}\left[-2\xi+3\xi^2+\xi\lambda\right]. \end{aligned} \tag{A.2}$$

where the coefficient ξ is equal to s/l_s, and λ is the shear effect coefficient, satisfying $\lambda = 12E_sI_s/K_s^{'}A_sG_sl_s^2$.

$$B_1(s) = \frac{\partial N_1(s)}{\partial s}, B_4(s) = \frac{\partial N_4(s)}{\partial s}, B_5(s) = \frac{\partial N_5(s)}{\partial s}, B_8(s) = \frac{\partial N_8(s)}{\partial s}. \tag{A.3}$$

$$R_1(s) = \frac{\partial D_1(s)}{\partial s}, R_4(s) = \frac{\partial D_4(s)}{\partial s}, R_5(s) = \frac{\partial D_5(s)}{\partial s}, R_8(s) = \frac{\partial D_8(s)}{\partial s}. \tag{A.4}$$

The specific expressions of $U_1^T/\partial q_s$, $U_2^T/\partial q_s$ and $U_3^T/\partial q_s$ are:

$$\begin{cases}\frac{\partial U_1^T}{\partial x_1}=\frac{1}{4}N^T\int_0^{l_s}[2D_1(s)(D_1(s)x_1+D_4(s)\varphi_1+D_5(s)x_2+D_8(s)\varphi_2)]ds,\\ \frac{\partial U_1^T}{\partial y_1}=\frac{1}{4}N^T\int_0^{l_s}[2D_1(s)(D_1(s)y_1-D_4(s)\theta_1+D_5(s)y_2-D_8(s)\theta_2)]ds,\\ \frac{\partial U_1^T}{\partial \theta_1}=\frac{1}{4}N^T\int_0^{l_s}[2D_4(s)(-D_1(s)y_1+D_4(s)\theta_1-D_5(s)y_2+D_8(s)\theta_2)]ds,\\ \frac{\partial U_1^T}{\partial \varphi_1}=\frac{1}{4}N^T\int_0^{l_s}[2D_4(s)(D_1(s)x_1+D_4(s)\varphi_1+D_5(s)x_2+D_8(s)\varphi_2)]ds,\\ \frac{\partial U_1^T}{\partial x_2}=\frac{1}{4}N^T\int_0^{l_s}[2D_5(s)(D_1(s)x_1+D_4(s)\varphi_1+D_5(s)x_2+D_8(s)\varphi_2)]ds\\ \frac{\partial U_1^T}{\partial y_2}=\frac{1}{4}N^T\int_0^{l_s}[2D_5(s)(D_1(s)y_1-D_4(s)\theta_1+D_5(s)y_2-D_8(s)\theta_2)]ds,\\ \frac{\partial U_1^T}{\partial \theta_2}=\frac{1}{4}N^T\int_0^{l_s}[2D_8(s)(-D_1(s)y_1+D_4(s)\theta_1-D_5(s)y_2+D_8(s)\theta_2)]ds,\\ \frac{\partial U_1^T}{\partial \varphi_2}=\frac{1}{4}N^T\int_0^{l_s}[2D_8(s)(D_1(s)x_1+D_4(s)\varphi_1+D_5(s)x_2+D_8(s)\varphi_2)]ds.\end{cases} \tag{A.5}$$

$$\begin{aligned}&\frac{\partial U_2^T}{\partial x_1}=-\frac{1}{2}M_x^T\int_0^{l_s}R_1ds,\ \frac{\partial U_2^T}{\partial y_1}=0,\ \frac{\partial U_2^T}{\partial \theta_1}=0,\ \frac{\partial U_2^T}{\partial \varphi_1}=-\frac{1}{2}M_x^T\int_0^{l_s}R_4ds,\\ &\frac{\partial U_2^T}{\partial x_2}=-\frac{1}{2}M_x^T\int_0^{l_s}R_5ds,\ \frac{\partial U_2^T}{\partial y_2}=0,\ \frac{\partial U_2^T}{\partial \theta_2}=0,\ \frac{\partial U_2^T}{\partial \varphi_2}=-\frac{1}{2}M_x^T\int_0^{l_s}R_8ds.\end{aligned} \tag{A.6}$$

$$\begin{aligned}&\frac{\partial U_3^T}{\partial x_1}=0,\ \frac{\partial U_3^T}{\partial y_1}=-\frac{1}{2}M_y^T\int_0^{l_s}R_1ds,\ \frac{\partial U_3^T}{\partial \theta_1}=\frac{1}{2}M_y^T\int_0^{l_s}R_4ds,\ \frac{\partial U_3^T}{\partial \varphi_1}=0,\\ &\frac{\partial U_3^T}{\partial x_2}=0,\ \frac{\partial U_3^T}{\partial y_2}=-\frac{1}{2}M_y^T\int_0^{l_s}R_5ds,\ \frac{\partial U_3^T}{\partial \theta_2}=\frac{1}{2}M_y^T\int_0^{l_s}R_8ds,\ \frac{\partial U_3^T}{\partial \varphi_2}=0.\end{aligned} \tag{A.7}$$

The stiffness matrix caused by temperature stress is expressed as:

$$[K]_T^e=\frac{1}{2}N^T\int_0^{l_s}\begin{bmatrix} D_1^2 & 0 & 0 & D_1D_4 & D_1D_5 & 0 & 0 & D_1D_8\\ 0 & D_1^2 & -D_1D_4 & 0 & 0 & D_1D_5 & -D_1D_8 & 0\\ 0 & -D_1D_4 & D_4^2 & 0 & 0 & -D_4D_5 & D_4D_8 & 0\\ D_1D_4 & 0 & 0 & D_4^2 & D_4D_5 & 0 & 0 & D_4D_8\\ D_1D_5 & 0 & 0 & D_4D_5 & D_5^2 & 0 & 0 & -D_5D_8\\ 0 & D_1D_5 & -D_4D_5 & 0 & 0 & D_5^2 & -D_5D_8 & 0\\ 0 & -D_1D_8 & D_4D_8 & 0 & 0 & -D_5D_8 & D_8^2 & 0\\ D_1D_8 & 0 & 0 & D_4D_8 & D_5D_8 & 0 & 0 & D_8^2\end{bmatrix}ds. \tag{A.8}$$

Data availability

No data was used for the research described in the article.

References

[1] H.H. Yoo, J. Hun Park, J. Park, Vibration analysis of rotating pre-twisted blades, Comput. Struct. 79 (19) (2001) 1811–1819, https://doi.org/10.1016/S0045-7949(01)00110-9.
[2] Y.J. Chiu, S.C. Huang, The influence on coupling vibration of a rotor system due to a mistuned blade length, Int. J. Mech. Sci. 49 (4) (2007) 522–532, https://doi.org/10.1016/j.ijmecsci.2006.05.016.
[3] S.C. Huang, Y.J. Chiu, Y.J. Lu, Damping property and vibration analysis of blades with viscoelastic layers, J. Syst. Des. Dyn. 1 (2) (2007) 340–351, https://doi.org/10.1299/jsdd.1.340.
[4] J. Sun, I.L. Arteaga, L. Kari, General shell model for a rotating pretwisted blade, J. Sound. Vib. 332 (22) (2013) 5804–5820, https://doi.org/10.1016/j.jsv.2013.06.025.
[5] C.F. Li, H.X. She, W. Lin, B.C. Wen, The influence of shaft's bending on the coupling vibration of a flexible blade-rotor system, Math. Probl. Eng. (2017), https://doi.org/10.1155/2017/7313956.
[6] H.X. She, C.F. Li, Q.S. Tang, B.C. Wen, The investigation of the coupled vibration in a flexible-disk blades system considering the influence of shaft bending vibration, Mech. Syst. Signal. Proc. 111 (2018) 545–569, https://doi.org/10.1016/j.ymssp.2018.03.044.
[7] H.X. She, C.F. Li, Q.S. Tang, B.C. Wen, Effects of blade's interconnection on the modal characteristics of a shaft-disk-blade system, Mech. Syst. Signal. Proc. 146 (2021) 106955, https://doi.org/10.1016/j.ymssp.2020.106955.
[8] L.H. Yang, Z. Mao, X.F. Chen, R.Q. Yan, J.S. Xie, H.F. Hu, Dynamic coupling vibration of rotating shaft–disc–blade system — Modeling, mechanism analysis and numerical study, Mech. Mach. Theory 167 (2022) 104542, https://doi.org/10.1016/j.mechmachtheory.2021.104542.
[9] H.X. She, C.F. Li, G.B. Zhang, Q.S. Tang, Investigation on the parameter sensitivity of bladed assemblies undergoing mistuning features, Appl. Acoust. 178 (2021) 107998, https://doi.org/10.1016/j.apacoust.2021.107998.
[10] M. Sekkal, R. Bachir Bouiadjra, S. Benyoucef, A. Tounsi, M.H. Ghazwani, A. Alnujaie, Investigation on static stability of bidirectional FG porous beams exposed to variable axial load, Acta Mech. 234 (3) (2023) 1239–1257, https://doi.org/10.1007/s00707-022-03370-9.
[11] M.S. Alves, R.N. Monteiro, Stability for a composite of Timoshenko laminated beams, J. Evol. Equ. 23 (4) (2023) 63, https://doi.org/10.1007/s00028-023-00911-0.
[12] B. Uzun, Ö. Civalek, M.Ö. Yaylı, Vibration of FG nano-sized beams embedded in Winkler elastic foundation and with various boundary conditions, Mech. Based. Des. Struc. 51 (1) (2023) 481–500, https://doi.org/10.1080/15397734.2020.1846560.
[13] M. Mohammadimehr, S. Alimirzaei, Buckling and free vibration analysis of tapered FG- CNTRC micro Reddy beam under longitudinal magnetic field using FEM, Smart. Struct. Syst. 19 (3) (2017) 309–322, https://doi.org/10.12989/SSS.2017.19.3.309.
[14] M. Ermis, A. Kutlu, N. Eratlı, M.H. Omurtag, Free vibration of axially FG curved beam on orthotropic Pasternak foundation via mixed FEM, J. Braz. Soc. Mech. Sci. Eng. 44 (12) (2022) 597, https://doi.org/10.1007/s40430-022-03853-9.
[15] X. Liu, A. Pagani, E. Carrera, X. Liu, Free vibration analysis of composite beams and laminated reinforced panels by refined dynamic stiffness method and CUF-based component-wise theory, Compos. Struct. 337 (2024) 118058, https://doi.org/10.1016/j.compstruct.2024.118058.
[16] E. Carrera, M.D. Demirbas, Evaluation of bending and post-buckling behavior of thin-walled FG beams in geometrical nonlinear regime with CUF, Compos. Struct. 275 (2021) 114408, https://doi.org/10.1016/j.compstruct.2021.114408.
[17] B.V. Sankar, J.T. Tzeng, Thermal Stresses in functionally graded beams, AIAA J. 40 (6) (2002) 1228–1232, https://doi.org/10.2514/2.1775.
[18] Y. Fu, J. Wang, Y. Mao, Nonlinear analysis of buckling, free vibration and dynamic stability for the piezoelectric functionally graded beams in thermal environment, Appl. Math. Model. 36 (9) (2012) 4324–4340, https://doi.org/10.1016/j.apm.2011.11.059.
[19] M. Aouadi, Stability analysis in extensible thermoelastic beam with microtemperatures, Z. Angew. Math. Phys. 74 (3) (2023) 86, https://doi.org/10.1007/s00033-023-01979-x.
[20] M. Alimoradzadeh, H. Heidari, F. Tornabene, R. Dimitri, Thermo-Mechanical buckling and non-linear free oscillation of functionally graded fiber-reinforced composite laminated (FG-FRCL) beams, Appl. Sci. 13 (8) (2023) 4904, https://doi.org/10.3390/app13084904.
[21] A. Paul, D. Das, Non-linear thermal post-buckling analysis of FGM Timoshenko beam under non-uniform temperature rise across thickness, Eng. Sci. Technol. 19 (3) (2016) 1608–1625, https://doi.org/10.1016/j.jestch.2016.05.014.
[22] S. Nesarhosseini, R. Ansari, M. Faraji Oskouie, H. Rouhi, Thermally induced vibration analysis of Timoshenko beams based on the micropolar thermoelasticity, Acta. Mech. 234 (5) (2023) 1957–1971, https://doi.org/10.1007/s00707-022-03455-5.
[23] L. Gu, Z. Qin, F. Chu, Analytical analysis of the thermal effect on vibrations of a damped Timoshenko beam, Mech. Syst. Signal. Proc. 60–61 (2015) 619–643, https://doi.org/10.1016/j.ymssp.2014.11.014.
[24] S.E. Ghiasian, Y. Kiani, M.R. Eslami, Nonlinear thermal dynamic buckling of FGM beams, Eur. J. Mech. A-Solid. (2015), https://doi.org/10.1016/j.euromechsol.2015.07.004.
[25] Y. Fu, J. Wang, S. Hu, Analytical solutions of thermal buckling and postbuckling of symmetric laminated composite beams with various boundary conditions, Acta. Mech. 225 (1) (2014) 13–29, https://doi.org/10.1007/s00707-013-0941-z.
[26] A. Mahi, E.A. Adda Bedia, A. Tounsi, I. Mechab, An analytical method for temperature-dependent free vibration analysis of functionally graded beams with general boundary conditions, Compos. Struct. 92 (8) (2010) 1877–1887, https://doi.org/10.1016/j.compstruct.2010.01.010.
[27] S.K. Simonetti, G. Turkalj, D. Lanc, Thermal buckling analysis of thin-walled closed section FG beam-type structures, Thin Wall. Struct. 181 (2022) 110075, https://doi.org/10.1016/j.tws.2022.110075.
[28] S.R. Li, F. Zhang, R.C. Batra, Thermoelastic damping in high frequency resonators using higher-order shear deformation theories, Thin Wall Struct. 188 (2023) 110778, https://doi.org/10.1016/j.tws.2023.110778.
[29] M. Marin, H. Aatef, A. Ibrahim, The effects of fractional time derivatives in porothermoelastic materials using finite element method, Math 9 (14) (2021) 1606, https://doi.org/10.3390/math9141606.
[30] M. Marin, S. Aly, V. Sorin, C. Adina, On mixed problem in thermoelasticity of type III for Cosserat media, J. Taibah. Univ. Sci. 16 (1) (2022) 1264–1274, https://doi.org/10.1080/16583655.2022.2160290.
[31] M. Marin, O. Andreas, M.I.A. Othman, On the evolution of solutions of mixed problems in thermoelasticity of porous bodies with dipolar structure, Continuum. Mech. Therm. 34 (2) (2022) 491–506, https://doi.org/10.1007/s00161-021-01066-4.
[32] J. Fang, B. Yin, X. Zhang, Size-dependent vibrations of porous functionally graded rotating microplates under thermal environment, Eur. J. Mech. A-Solid 95 (2022) 104645, https://doi.org/10.1016/j.euromechsol.2022.104645.
[33] K. Liang, Z. Wang, A highly efficient and accurate FE-ROM method for thermal-mechanical buckling of heat transfer panels, Aerosp. Sci. Technol. 129 (2022) 107838, https://doi.org/10.1016/j.ast.2022.107838.
[34] B. Zhang, Y. Li, W.Z. Lu, Dynamic characteristics of rotating pretwisted clamped-clamped beam under thermal stress, J. Mech. Sci. Technol. 30 (9) (2016) 4031–4042, https://doi.org/10.1007/s12206-016-0816-z.
[35] Y.Z. Zhao, Y.J. Chiu, C.H. Yang, G.F. Yu, Research on heat-elastic coupled vibration in a rotating rigid disk rotor system, J. Mech. Sci. Technol. 36 (4) (2022) 1667–1678, https://doi.org/10.1007/s12206-022-0109-7.
[36] Y.J. Chiu, Y.Z. Zhao, D. Chen, C.H. Yang, Analytical, numerical, and experimental methods to study thermo-elastic coupling inherent and vibration characteristics of a flexible rotor system, J. Vib. Control (2023), https://doi.org/10.1177/10775463231187009.

[37] H. Guo, X. Ouyang, K.K. Żur, X. Wu, T. Yang, A.J.M. Ferreira, On the large-amplitude vibration of rotating pre-twisted graphene nanocomposite blades in a thermal environment, Compos. Struct. 282 (2022) 115129, https://doi.org/10.1016/j.compstruct.2021.115129.

[38] Gh. Shabanlou, S.A.A. Hosseini, M. Zamanian, Vibration analysis of FG spinning beam using higher-order shear deformation beam theory in thermal environment, Appl. Math. Model. 56 (2018) 325–341, https://doi.org/10.1016/j.apm.2017.11.021.

[39] Y.W. Kim, Temperature dependent vibration analysis of functionally graded rectangular plates, J. Sound. Vib. 284 (3–5) (2005) 531–549, https://doi.org/10.1016/j.jsv.2004.06.043.

[40] O. Kauss, H. Tsybenko, K. Naumenko, S. Hütter, M. Krüger, Structural analysis of gas turbine blades made of Mo-Si-B under transient thermo-mechanical loads, Comp. Mater. Sci. 165 (2019) 129–136, https://doi.org/10.1016/j.commatsci.2019.04.023.

[41] P. Malekzadeh, M.R. Golbahar Haghighi, M.M. Atashi, Out-of-plane free vibration of functionally graded circular curved beams in thermal environment, Compos. Struct. 92 (2) (2010) 541–552, https://doi.org/10.1016/j.compstruct.2009.08.040.

[42] Y. Guo, L. Li, D. Zhang, Dynamic modeling and vibration analysis of rotating beams with active constrained layer damping treatment in temperature field, Compos. Struct. 226 (2019) 111217, https://doi.org/10.1016/j.compstruct.2019.111217.

[43] H.D. Nelson, A finite rotating shaft element using Timoshenko beam theory, J. Mech. Design. 102 (4) (1980) 793–803, https://doi.org/10.1115/1.3254824.

[44] A.D. Hobiny, I.A. Abbas, Nonlinear analysis of dual-phase lag bio-heat model in living tissues induced by laser irradiation, J. Therm. Stresses. 43 (4) (2020) 503–511, https://doi.org/10.1080/01495739.2020.1722050.